JOURNAL OF MATERIALS SCIENCE 22 (1987) 2542–2548

The structure of a cast dental Ni–Cr–Be alloy

H. HERØ
NIOM – Scandinavian Institute of Dental Materials, Oslo, Norway
E. SØRBRØDEN, J. GJØNNES
Department of Physics, University of Oslo, Oslo, Norway

The structure of a typical dental Ni–Cr–Be alloy with 1.8 wt% Be has been investigated by SEM and TEM as well as by quantitative X-ray microanalyses in both instruments. Due to its low atomic weight the atomic fraction of Be is as high as 0.10. During solidification beryllium segregates substantially, and a large volume fraction of the casting is made up of a eutectic with coarse (≈ 1 μm diameter) alternating rods of f c c Ni–Cr and NiBe with a CsCl-type structure (ordered b c c). Smaller (≈ 0.1 μm diameter) rods of NiBe are precipitated in matrix in the solid state. Microanalyses of the NiBe rods show that they have a low chromium content (≈ 1.5 wt%). The cube boundary planes of the ordered b c c and f c c structures have a slight difference in orientation of about 7° which is most probably due to a small coherency misfit of the two types of lattices. The ⟨1 0 0⟩ directions in cube boundary plane of the f c c structure are nearly parallel to the ⟨1 1 0⟩ directions of the ordered b c c cube boundary plane. Sometimes another and more complex relationship between the two lattices occurs. The alloy contains 3.9 wt% Al which gives rise to numerous small (≈ 10 nm), spherical, ordered particles of Ni_3Al both in matrix as well as in the f c c eutectic rods.

1. Introduction

Castings of Ni–Cr–Be alloys have recently become widely used, particularly in North America, as a material for fixed prosthetic restorations. The corrosion resistance is provided primarily by chromium and to some extent by molybdenum, because of dense oxide films. Beryllium reduces the solidification temperatures and possibly it also increases the castability of the alloy [1, 2]. Furthermore, beryllium is claimed to improve the bond strength between the alloy substrate and the ceramic veneer [3]. The disadvantage of beryllium is its well known toxic effects, in particular by inhalation of fumes and dust [2].

The content of beryllium in dental Ni–Cr alloys is normally in the range of 1.5 to 2 wt %. Due to its low atomic weight, however, this corresponds to approximately 10 at %. Thus the influence of beryllium on the solidification pattern and on the alloy structure have been reported to be be significant [4, 5].

The dendritic arms are predominantly f c c Ni–Cr. Interdendritically as well as at grain boundaries eutectic particles consisting alternatingly of lamellae or rods similar to the Ni–Cr matrix and NiBe have been observed [5]. This solidification pattern can be expected from the Ni–Be binary phase diagram (Fig. 1) [6] and a non-equilibrium solidification of an alloy with a composition of approximately 10 at % Be. Furthermore, microprobe measurements have shown the NiBe-phase to be chromium depleted [7]. Corrosion tests reveal this phase to be less resistant than the matrix [7]. When aluminium is present, small coherent Ni_3Al particles (γ') appear in the matrix [5].

A proper knowledge of the structure and the way it is created during casting are important for an improved understanding of the corrosion resistance and mechanical properties of a Ni–Cr–Be alloy. The aim of the present work was to obtain improved information about the structure and compositions of the phases in a casting of a typical commercial dental Ni–Cr–Be alloy by means of scanning electron microscopy (SEM), transmission electron microscopy (TEM) and quantitative X-ray microanalysis in both instruments.

2. Materials and methods

A plate 20 × 20 × 1 mm was cast of the alloy Rexillium III (Jeneric Industries Inc, Wallingford, Connecticut, USA) in an induction casting machine (Linn Elektronik Induktherm HFS-3 Vac, FRG) using argon atmosphere and a phosphate bonded investment (Aurovest soft, BEGO; Bremer Goldschlägerei, Wilh. Herbst GmbH) preheated to 900° C. The casting was heated so as to simulate the firing of opaque and body ceramic (Ceramco) as well as the final glazing. Two parallel 5 × 5 mm specimens were cut from the heat treated casting and prepared by grinding and polishing using standard metallographic techniques. Finally a thin film of carbon was evaporated onto the surface of the specimens prior to investigations in a combined SEM and X-ray microprobe instrument (Camebax Microbeam, Cameca, Paris) equipped with wavelength dispersive spectrometers (WDS). Three parallel measurements were made of each type of structural detail.

Three specimens for TEM and X-ray microanalysis were cut from the as-cast and heat treated sample and ground to a thickness of approximately 50 μm. Subsequently they were thinned electrolytically in a jet

0022–2461/87 $03.00 + .12

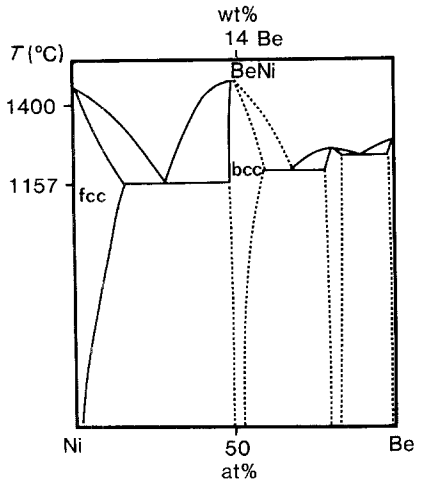

Figure 1 The Ni–Be binary phase diagram [6].

polishing apparatus using a solution consisting of 25% HNO_3 in CH_3OH at $-30°$ C. Finally, ion beam thinning was carried out.

The foils were examined in a transmission electron microscope (JEM 2000 FX), equipped with a double tilt holder and an X-ray detector and analyser (Tractor Northern 2000, Wisconsin, USA). X-ray energy dispersive spectroscopy (EDS) with a high angle detector was carried out in the TEM mode using a spot size of 20 to 50 nm.

The chemical compositions from the EDS-analyses in the TEM of the eutectic rod and matrix are given in Table I (three parallel measurements of each type of structural detail). The thin film approximation was used in calculating the chemical compositions [8]:

$$\frac{C_A}{C_B} = k_{A,B} \frac{I_A}{I_B} \quad (1)$$

where C_A and C_B are weight fractions of the elements A and B, I_A and I_B their corresponding X-ray intensities and $K_{A,B}$ is a correction factor. In the present experiments nickel was chosen as the reference element B. The intensity of K_α-lines was used in the calculations.

The X-ray detector in the TEM instruments is equipped with computer and software. The correction factors were calculated according to Goldstein [8]. The following values were derived: $K_{Cr} = 0.8574$, $K_{Al} = 1.058$ and $L_{Mo} = 2.8514$.

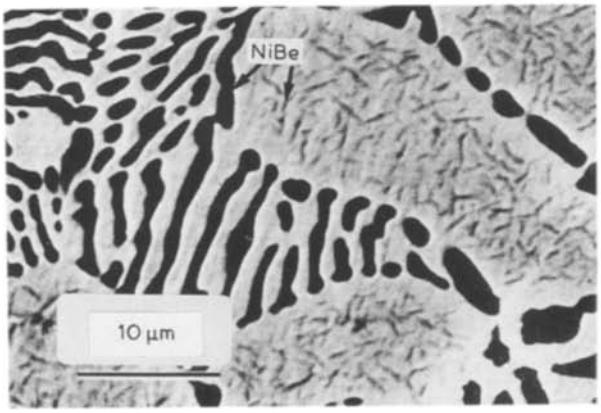

Figure 2 SEM micrograph of the NiCrBe as-cast alloy, displaying dendrite arms and eutectic area. Back scattering electrons.

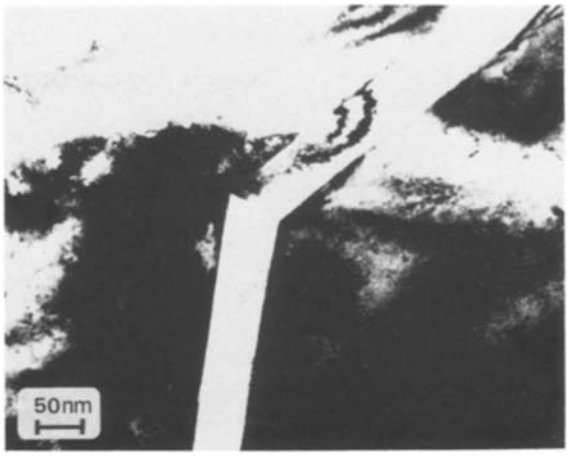

Figure 3 TEM (bright field image) of matrix with two NiBe rods precipitated in the solid state. Note the nonequivalent orientations of the rods relative to the surrounding grain.

The chemical composition of the alloy was determined by atomic absorption analysis (carried out at the Center for Industrial Research, Oslo). Carbon was analysed by combustion to CO_2 and subsequent coulometric titration (carried out at Elkem A/S, Oslo).

3. Results

The atomic absorption analyses revealed that the alloy contains (in wt %): 13.5% Cr, 2.1% Mo, 3.9% Al, 0.35% Ti, 0.36% Co, 0.12% Cu and 0.1% Si. The carbon content was found to be 0.014 wt %. According to the manufacturer the alloy contains 1.8 wt % Be.

The SEM micrograph in Fig. 2 displays eutectic areas consisting of coarse (1 to 2 µm) dark and bright rods embedded in a matrix containing numerous faint traces of small, rod-shaped precipitates. The wavelength dispersive microprobe analysis of matrix and the eutectic rods are given in Table I. The dark rods were found to be chromium depleted. Beryllium could not be determined due to its low atomic weight, but the concentration of this element in the matrix and in the dark rods can be estimated to be 0 and 10 wt %, respectively, on the basis of the sum of the other observed elements (Table I).

The many small rods in the matrix (Fig. 2) appear

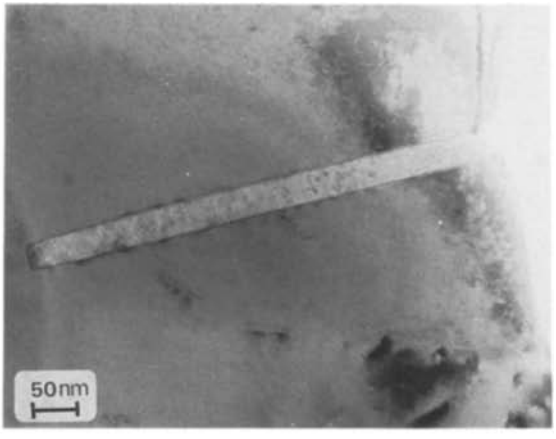

Figure 4 Area with an NiBe rod in matrix used for obtaining an SADP.

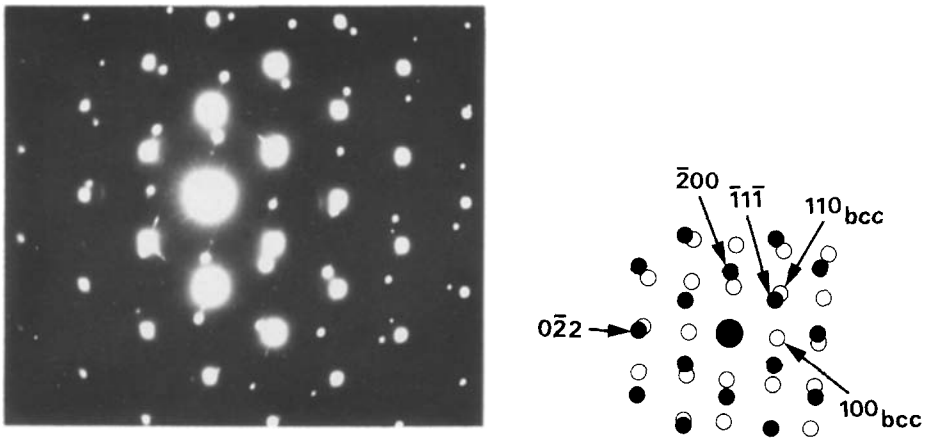

Figure 5 SADP from area shown in Fig. 4. ●, NiCr fcc [0 1 1] zone axis; ○, NiBe bcc [0 0 1] zone axis.

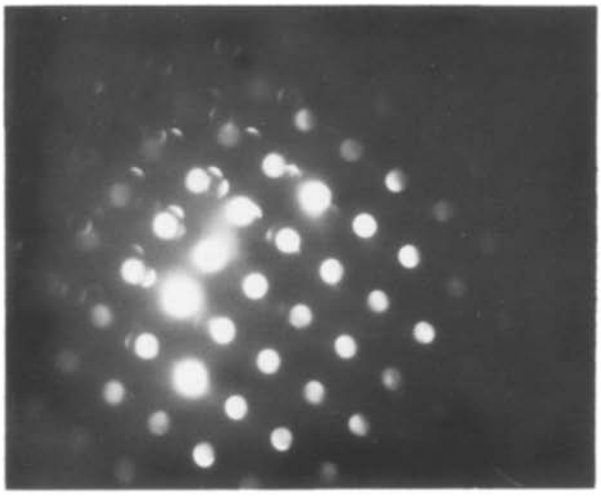

Figure 6 Microdiffraction pattern (CsCl-type, [0 0 1] zone axis) of the lower of the two legs shown in Fig. 3.

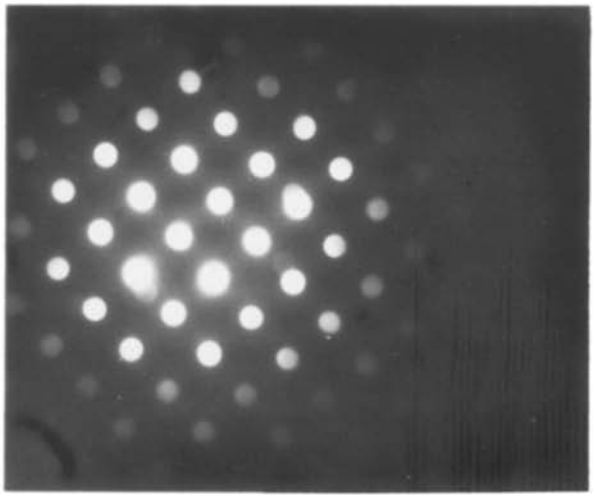

Figure 7 Microdiffraction pattern (CsCl-type, [0 0 1] zone axis) of the upper of the two legs shown in Fig. 3.

in TEM as straight needles of thickness 20 to 50 nm (Figs 3 and 4). Two different nonequivalent orientations relative to the matrix grain are seen. Occasionally, these two are joined together as in Fig. 3. The diffraction pattern in Fig. 5 from a single rod (Fig. 4) was indexed according to the CsCl-type lattice with a lattice constant 0.257 nm in good agreement with the reported structure of NiBe [6]. For the fcc NiCr matrix (Fig. 5) the lattice constant was determined to be 0.355 nm; the value 0.352 nm is given in the literature for nickel [9].

The orientation relationship between the two lattices in Fig. 5 was found to be

$$[0\,1\,1]_{NiCr} \| [0\,0\,1]_{NiBe}$$

$$(0\,\bar{1}\,1)_{NiCr} \| (0\,1\,0)_{NiBe}$$

with the length axis of the rod along the $\langle 0\,1\,0 \rangle$ direction of its ordered bcc structure. A small rotation

TABLE I Composition of structural components measured by WDS* and EDS†

Element		fcc matrix		Eutectic fcc rods		Eutectic NiBe rods		NiBe rods in matrix	
		x	S.D.	x	S.D.	x	S.D.	x	S.D.
Nickel	WDS	78.9	0.3	78.5	0.5	87.8	0.7	–	
	EDS	77.2	1.2	76.4	1.1	87.6‡	1.0	87.3†	1.3
Chromium	WDS	15.6	0.07	14.8	0.4	1.3	0.1	–‡	
	EDS	15.2	1.0	15.4	0.4	1.2‡	0.2	2.2†	
Molybdenum	WDS	5.4	0.2	6.7	0.5	0.2	0.1	–	
	EDS	5.3	1.0	6.6	0.9	0.9‡	0.7	–	
Aluminium	WDS	2.8	0.01	2.9	0.01	0.35	0.02	–	
	EDS	2.0	0.65	1.4	0.9	0.3‡	0.2	0.4‡	0.7
Total	WDS	102.6		102.8		89.6		89.9	

*Wave length dispersive X-ray spectrography (in a combined SEM and microprobe instrument).
†Energy dispersive X-ray spectrography (in TEM).
‡In calculating the composition of bcc rods on the basis of EDS measurements in TEM, a beryllium content of 10 wt % was assumed according to the total sum of other elements obtained by WDS for eutectic bcc rods.

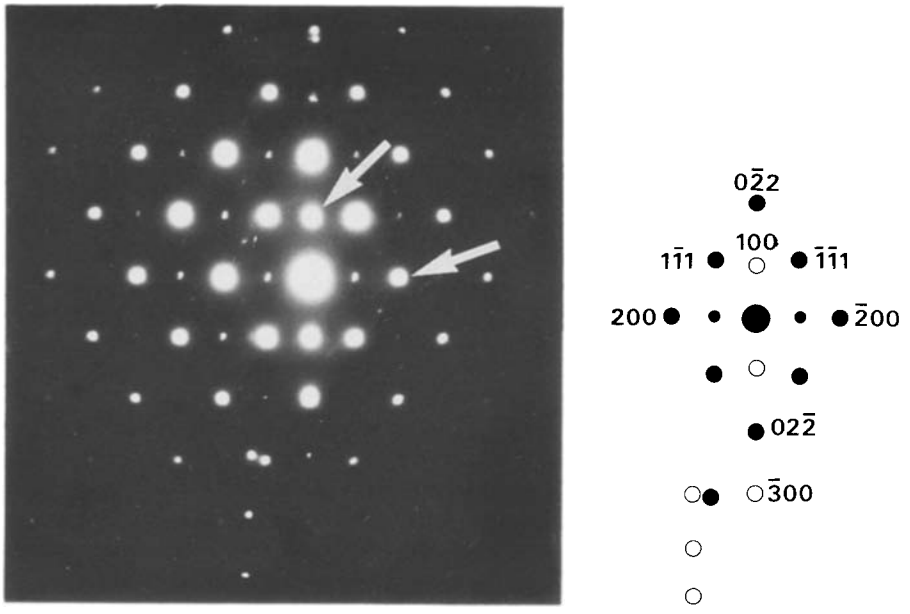

Figure 8 SADP of a eutectic area comprising alternating rods shown in Figs 9 and 10. ●, NiCr f c c [0 1 1] zone axis; ○, NiBe b c c [0 0 1] zone axis.

around the NiBe [0 0 1] axis is seen. Weak extra reflections from the matrix at f c c: 100 appear to originate from precipitates. Microdiffraction of each of the two legs of the precipitate in Fig. 3 as shown in Figs 6 and 7 reveal an angular difference of about 10° between the two b c c diffraction patterns around the [0 0 1] zone axis. One of the two legs is oriented with the length axis along the NiBe [0 1 0]. The other leg forms an angle about 45° with the [0 1 0] needle direction.

A diffraction pattern from the eutectic area (Fig. 8) reveals the same orientation relationship as above between the two lattices. Dark field pictures of the two types of reflections (Figs 9 and 10) show the two types of rods with characteristic facetted boundaries. The extra spots at $(1\,0\,0)_{fcc}$ etc. as for matrix in Fig. 5 are quite strong. A dark field picture (Fig. 12) from the same eutectic area taken from the superstructure reflection ($\bar{1}\,\bar{2}\,1$) in Fig. 11 shows a distribution of fine,

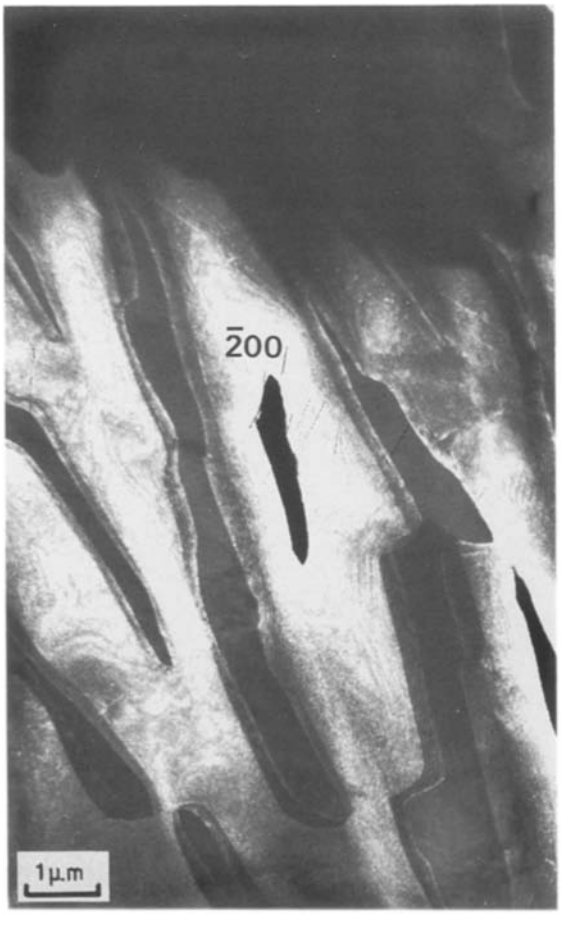

Figure 9 Dark field image using the (2 0 0) reflection of the f c c pattern in Fig. 8.

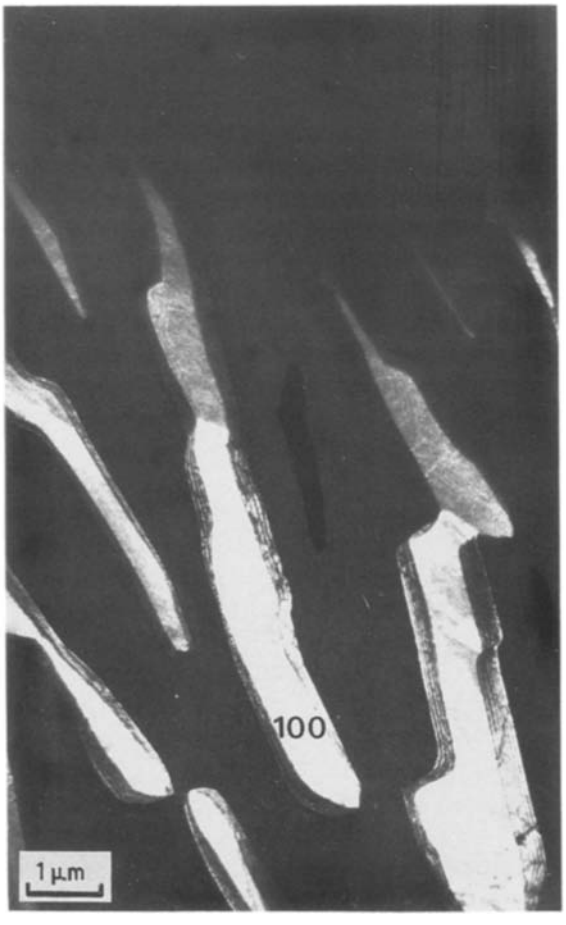

Figure 10 Dark field image using the (1 0 0) reflection of the b c c pattern in Fig. 8.

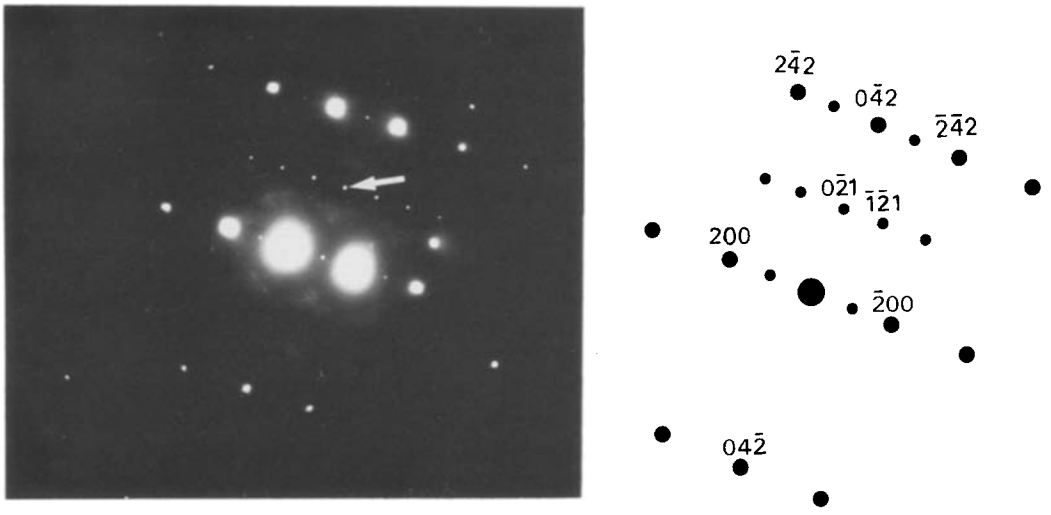

Figure 11 SADP from the same area as in Fig. 8, but with zone axis fcc [0 1 2].

apparently spherical precipitates. The pronounced thickness dependence of the contrast is due to the resence of a strong matrix reflection.

The chemical composition of the two sets of rods as well as of the matrix was determined with EDS analysis in TEM and with wavelength dispersion analysis in the microprobe. The two determinations agree well for all three microstructural elements (Table I). TEM analysis could be carried out also for the rods in the matrix, where a composition very similar to the beryllium-rich eutectic rods was found. In the WDS analyses, the beryllium-content can be estimated from the sums. In the TEM/EDS determinations, beryllium contents of 0 and 10%, respectively, in the two components were assumed.

Occasionally small $\approx 0.1\,\mu$m carbides could be observed in the matrix (Fig. 13). The corresponding diffraction pattern of the particle and the surrounding matrix (Fig. 14) shows that the particle is of the type $M_{23}C_6$ (M = chromium, molybdenum).

4. Discussion

The main microstructural feature of the cast alloy can be understood by reference to the Ni–Be binary phase diagram. During solidification beryllium segregates heavily toward interdendritic positions and grain boundaries, where the rest of the melt solidifies as an eutectic consisting of an fcc phase and a nearly stoichiomoteric NiBe phase with an ordered, CsCl-type structure. No clear evidence of segregation of the other elements during matrix solidification was found. They all had high solubility in the nickel matrix. In the eutectic these elements are seen to enter the fcc phase, the NiBe phase containing very little of the elements chromium, molybdenum and aluminium. The low chromium content is likely to be the explanation for the low corrosion resistance in these rods [7, 10]. For some unknown reason all the measured contents of aluminium (1.5 to 2.8 wt %) are too small compared with the bulk analysis (atomic absorption) of 3.9 wt %.

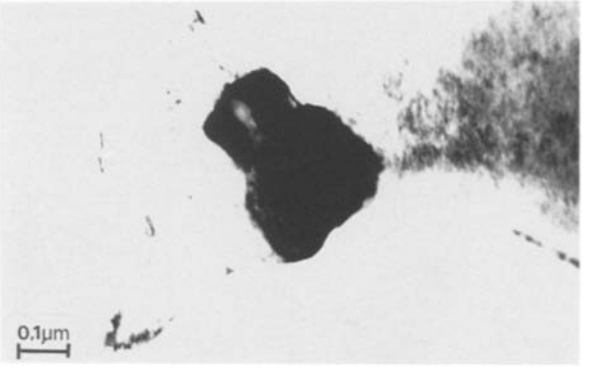

Figure 13 Dark field image of a $M_{23}C_6$ carbide in the matrix, using a superstructure reflection in Fig. 14.

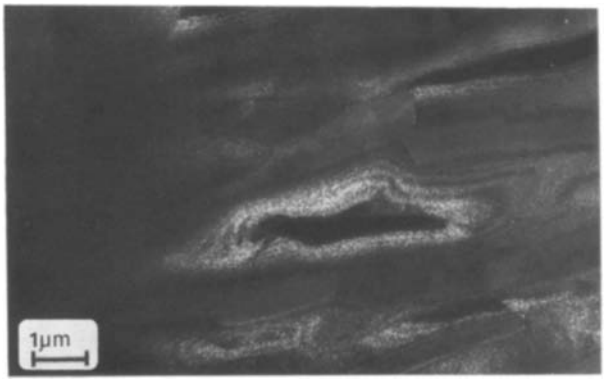

Figure 12 Dark field image using the ($\bar{1}\,\bar{2}$ 1) superstructure reflection in Fig. 11 of the fcc rods shown in Fig. 9, displaying numerous small, ordered Ni_3Al particles.

Figure 14 SADP of the $M_{23}C_6$ carbide particle and the surrounding matrix shown in Fig. 13. [0 0 1] Zone axis.

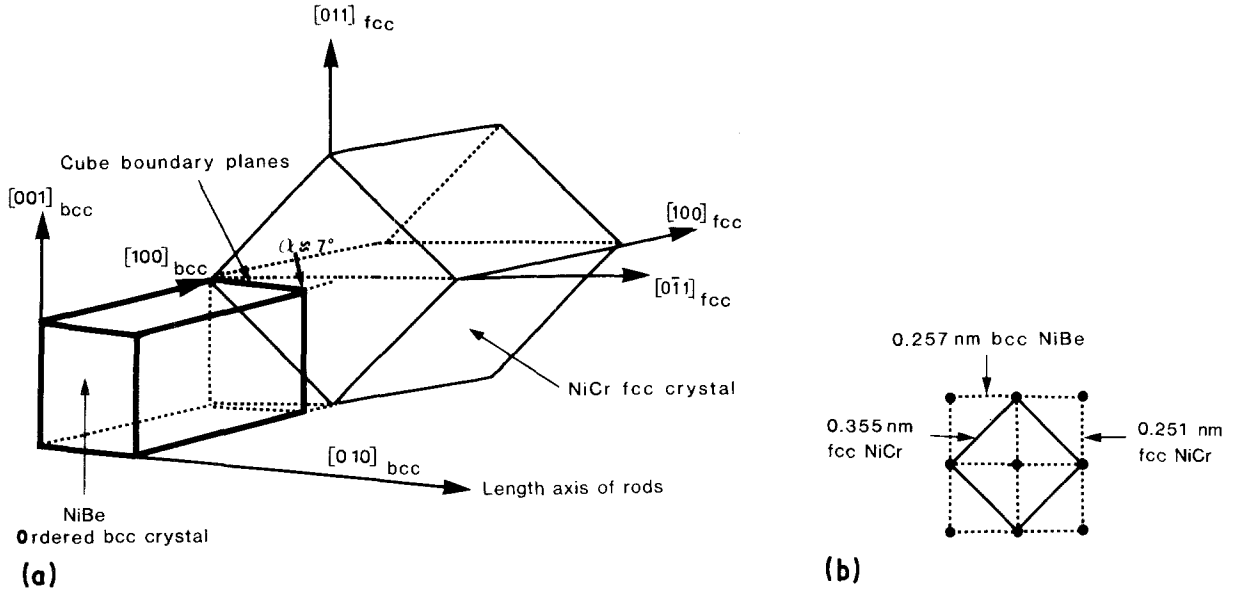

Figure 15 (a) Partial coherence of the fcc Ni–Cr and bcc NiBe lattice according to the SADP shown in Fig. 5. (b) Cube boundary planes of (···) ordered bcc, and (——) fcc crystals.

The finer rods or needles in the matrix are clearly a result of precipitation in the solid state. The rod in Fig. 4 can be seen to have been nucleated heterogeneously at the grain boundary.

The orientation relationship and the partial coherence between the fcc and the ordered bcc (NiBe) crystals indicated by the SADP in Fig. 5 are illustrated in Fig. 15. The atomic match at the boundary plane is good, but there is a discrepancy in spacing between neighbouring atoms of about 2 to 3%. This may be the reason for the observed slight deviation of about 7° for the two boundary planes.

As shown in Figs 2 and 3, there is also another orientation relationship occurring between the rods and the surrounding matrix crystal. The orientation difference in the surface plane between the length axis of the two rod orientations is approximately 45°. The two microdiffraction patterns in Figs 6 and 7 of the two legs of the particle in Fig. 3 are both that of NiBe (CsCl-type with [0 0 1] zone axis). However, an orientation difference of approximately 10° around the [0 0 1] axis between the two legs was observed. Furthermore, dark field imaging reveals the individual legs sometimes to be divided into several segments with only small angular differences. As illustrated in Fig. 16, the other orientation of the length axis of the needle lead to the possible boundary plane $(1\,1\,0)_{bcc}$ parallel to $(1\,1\,1)_{fcc}$. The match at this boundary will not be as good as for the orientation relationship indicated in Fig. 15.

The numerous small, spherical particles (Fig. 12) are most likely ordered ($L1_2$ type) Ni_3Al (γ') particles since nickel-based alloys with about 4% Al are known to contain such precipitates [5, 11]. The misfit of the lattice constants of the fcc Ni_3Al structure and matrix is only about 0.1% and allows homogeneous nucleation of a coherent precipitate with low surface energy [11]. For this reason the particles are small and contribute antiphase boundary strengthening to the alloy.

In a previous investigation of a similar alloy, but with a carbon content as high as 0.1 wt %, Cr_7C_3 particles were identified by electron diffraction of replicas [5]. In the present work, however, where the carbon content is as low as 0.014 wt %, occasional $M_{23}C_6$ carbides were found in the matrix. The carbides $Cr_{23}C_6$ is known to have a complex fcc unit cell with a length 1.0638 nm [12], which is three times the size of the fcc unit cell of the matrix. This relationship is supported by the SADP in Fig. 14 which also reveals coherency between the matrix and the carbide. The density of the observed $M_{23}C_6$ particles, however, is

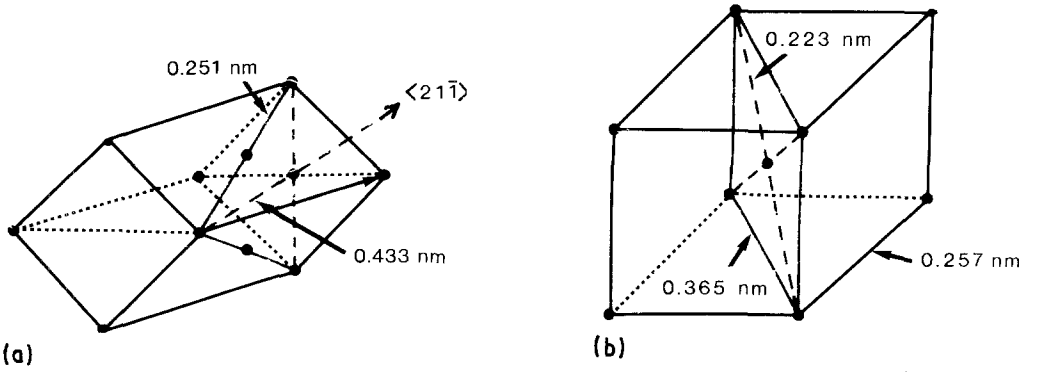

Figure 16 Suggested alternative boundary planes for (a) the fcc Ni–Cr (1 1 1) and (b) the ordered bcc (1 1 0) NiBe lattice based on rod orientations in Figs 2 and 3 relative to that indicated in Fig. 15.

too small to have a pronounced effect on the flow stress of the alloy.

References

1. R. P. WHITLOCK, R. W. HINMAN, G. T. EDEN, J. A. TESK, G. DICKSON and E. E. PARRY, *J. Dent. Res.* **60** (1981) 404.
2. K. J. ANUSAVICE (ed) "Report on base metal alloys for crown and bridge applications: benefits and risks", *J. Amer. Dent. Assoc.* **11** (1985) 479.
3. J. P. MOFFA, W. A. JENKINS, J. A. ELLISON and J. C. HAMILTON, *J. Prosthet Dent.* **52** (1984) 491.
4. G. R. BARAN, *ibid.* **50** (1983) 639.
5. J. M. HAUDIN, M. Y. PERRIN, M. DEGRANGE and G. BURDAIRON, in "Metallurgie Dentaire" (Pyc-édition, Paris, 1981) p. 50.
6. M. HANSEN and K. ANDERHOF, (eds), in "Constitution of Binary Alloys" (McGraw-Hill, New York, 1985) p. 290.
7. K. LUDWIG and J. BEHRENSDORF, *Dtsch. Zahnärztl. Z.* **33** (1978) 833.
8. J. I. GOLDSTEIN, in "Introduction to Analytical Microscopy", edited by J. J. Hren, J. I. Goldstein and D. C. Joy (Plenum Press, New York, 1979) p. 83.
9. C. S. BARRETT and T. B. MASSALSKI, "Structure of Metals" (Pergamon, Oxford, 1980) p. 628.
10. H. HERØ, J. VALDERHAUG and R. B. JØRGENSEN, *J. Dent. Res.* **65** (1986) abstract no. 1193.
11. C. T. SIMS and W. C. HAGEL, (eds), in "The Superalloys" (Wiley, New York, 1972) p. 43.
12. W. B. PEARSON, "Handbook of lattice spacings and structures of metals" (Pergamon, Oxford, 1958) p. 113.

Received 26 August
and accepted 9 October 1986